

Measuring a localization phase diagram controlled by the interplay of disorder and driving

Peter Dotti, Yifei Bai,* Toshihiko Shimasaki,* Anna R. Dardia, and David Weld†
Department of Physics, University of California, Santa Barbara, California 93106, USA
 (Dated: June 4, 2024)

The interplay of localizing and delocalizing mechanisms such as disorder, interactions, and driving is a central topic of modern condensed matter physics. In this work we experimentally explore the interplay between quasiperiodic disorder and periodic driving, each of which in isolation is capable of driving a metal-insulator phase transition. Using a 1D quasiperiodic cold-atom chain we measure transport across the full phase diagram varying both drive strength and quasi-disorder strength. We observe lobes of metallic phases bounded by quantum phase transitions which depend on both drive and disorder. While these observations are broadly consistent with expectations from a high-drive-frequency theoretical model, we also observe clear departures from the predictions of this model, including anomalous changes in localization behavior at lower drive frequency. We demonstrate experimentally and theoretically that understanding the full measured phase diagram requires an extension to commonly-used approximate theories of Floquet matter.

Due to the extended character of Bloch wavefunctions, quantum lattice systems tend to be metallic unless they are subjected to some localizing influence. Such influences include interactions (Mott localization), disorder (Anderson localization), quantum statistics (band insulators), and periodic driving (dynamic localization). The interplay of various localizing and delocalizing phenomena is a topic which remains at the forefront of the study of condensed matter, as evidenced for example by the recent intense investigation of the possible many-body localized state [1–4].

In this work, we experimentally and theoretically investigate the interplay of two independent localizing influences: periodic driving and quasiperiodic pseudo-disorder. A time-periodic driving force applied at specific amplitudes can cause dynamic localization by resonantly flattening out a Floquet band [5]. Separately, quasiperiodic pseudo-disorder can drive a localization-delocalization phase transition via Anderson-insulator-like interference effects, as expressed in the 1D Aubry-André-Harper (AAH) model [6–8]. This work aims to explore open questions concerning the application of *both* of these localizing influences to a quantum system: does the driving destroy the Anderson-like insulator? Can the quasi-disorder disrupt dynamical localization? What phase diagram arises from the interplay of the two effects? How is the phase diagram modified as the drive frequency approaches the bandwidth?

Previous work has theoretically explored transport in a driven disordered lattice [9–12] and experimentally investigated the effects of disorder in the vicinity of dynamic localization in waveguides [13]. These studies were generally restricted to the high-frequency limit.

The experiments we describe begin by loading a Bose-Einstein condensate of 8×10^4 ^{84}Sr atoms into a pair of superimposed 1D optical lattices with different spatial periods aligned along an axis perpendicular to gravity. The primary (secondary) lattice is formed by two

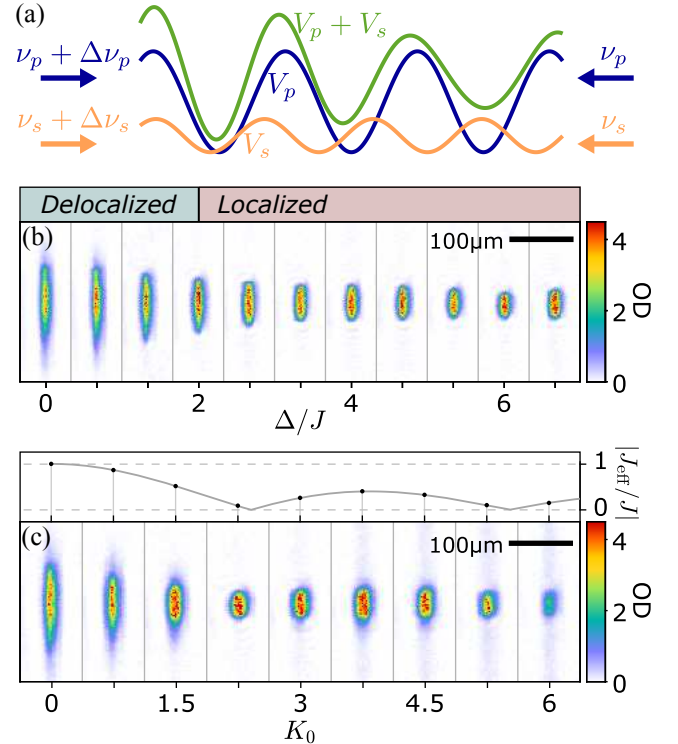


FIG. 1. Observing two kinds of localization. (a) Primary (blue) and secondary (orange) lattices combine to create a quasiperiodic potential (green) which can be translated via frequency modulation. (b) Atoms imaged after 500 ms hold time for different secondary lattice strengths demonstrate AAH localization at $\Delta/J > 2$. (c) Atoms imaged after 500 ms hold time for different drive strengths K demonstrate dynamic localization. Top panel indicates theoretically predicted $|J_{\text{eff}}|$. The lattice wavevector is in the vertical direction in (b) and (c).

counter-propagating beams of wavelength $\lambda_p = 1064$ nm ($\lambda_s = 874.61$ nm $\equiv \lambda_p/\beta$). All four beams pass through individual acousto-optic modulators. This allows for con-

trol of the lattice depths, denoted V_p and V_s for the primary and secondary lattices, and for synchronized translation of the lattices by setting frequency differences $\Delta\nu_p$ ($\Delta\nu_s$) between the two beams forming the primary (secondary) lattice (Fig. 1(a)). The resulting ability to rapidly tune the depth and spatial phase of both lattice potentials enables the simultaneous experimental realization of dynamic and quasisorder-induced localization. More experimental details appear in [14].

Synchronized sinusoidal lattice phase modulation is conveniently treated by transforming to the co-moving frame, in which the modulation appears as a time-varying electric field. We focus on the case where the secondary lattice is at rest in the co-moving frame of the primary lattice, implemented by fixing $\Delta\nu_s = \beta\Delta\nu_p$. This admits a description by the tight-binding Hamiltonian [11]

$$H = \sum_l -J(|l+1\rangle\langle l| + \text{h.c.}) + \Delta \cos(2\pi\beta l - \delta) |l\rangle\langle l| + \hbar\omega K_0 \cos(\omega t) l |l\rangle\langle l|, \quad (1)$$

where J is the tunneling energy, Δ is the quasisorder strength, K_0 is the dimensionless drive strength, $\beta = \lambda_p/\lambda_s = 1064/874.61$, and the phason parameter δ is constant. The tight-binding approximation is justified provided that V_p and V_p/V_s are sufficiently large, as is the case in our experiments [15, 16]. V_p is chosen to be $9E_{R,p}$, leading to $J = 0.0242E_{R,p}$, where $E_{R,p} = 2\pi^2\hbar^2/m\lambda_p^2$ is the recoil energy of the primary lattice. We explore a range of V_s values, from 0 up to $0.592E_{R,p}$.

Two special cases of Hamiltonian (1) correspond to the two localization mechanisms previously mentioned. When $K_0 = 0$, the Hamiltonian becomes the static AAH model. For irrational β [17], all eigenstates of this Hamiltonian exhibit a localization-delocalization quantum phase transition at $\Delta/J = 2$. Fig. 1(b) experimentally demonstrates the phase transition of the AAH model, showing *in situ* absorption images taken after 500 ms of expansion in the bichromatic lattice potential for $K_0 = 0$ with Δ/J values ranging from 0 to 6.7. As in Ref. [7], the phase transition is observed in the suppression of expansion for values of $\Delta/J > 2$. When $\Delta = 0$ in Hamiltonian (1), dynamic localization can occur [18–21]. Applying Floquet theory [22, 23] results in a modified tight-binding Hamiltonian with effective tunneling energy $J_{\text{eff}} = J\mathcal{J}_0(K_0)$ [18]. Crucially, hopping is entirely suppressed for dimensionless drive amplitudes corresponding to zeros of the Bessel function \mathcal{J}_0 , for example at $K_0 \approx 2.405$ and 5.520 . Fig. 1(c) shows *in situ* absorption images taken after 500 ms of expansion for varying drive amplitudes at $\Delta = 0$ and $\omega = 2\pi \times (1 \text{ kHz}) = 19.7J/\hbar$. Expansion is initiated by sudden removal of a confining optical dipole trap, simultaneous with the beginning of sinusoidal phase modulation. These data clearly demonstrate the suppression of

transport due to dynamic localization for K_0 close to the zeroes of $\mathcal{J}_0(K_0)$.

Having demonstrated that the experimental system can exhibit both quasisorder-induced localization and drive-induced localization, we proceed to investigate the main topic of this work, which is the interplay of these two phenomena. We measured the width of the atomic density distribution after 500 ms of expansion, with quasisorder strength Δ and drive amplitude K_0 independently varied to map out a 2D parameter space. Figs. 2(a) and (b) present experimental measurements of the localization phase diagram for a drive frequency of 1 kHz ($\hbar\omega = 19.7J$) and 200 Hz ($\hbar\omega = 3.9J$), respectively. For comparison, Figs. 2(c) and 2(d) present numerical calculations of the average inverse participation ratio (IPR) of the Floquet eigenstates.

The basic structure of Fig 2(a) and (c) can be best understood by the time-averaged Hamiltonian:

$$H_{\text{eff}} \approx \sum_l -J_{\text{eff}}(|l+1\rangle\langle l| + \text{h.c.}) + \Delta \cos(2\pi\beta l - \delta) |l\rangle\langle l| \quad (2)$$

which holds in the high-frequency approximation $\hbar\omega \gg 4J, 2\Delta$. Eq (2) is the AAH model with a Bessel-renormalized hopping amplitude J_{eff} . Thus, the localization phase transition occurs at $\Delta_c = 2|J_{\text{eff}}| = 2|J\mathcal{J}_0(K_0)|$. This theoretically predicted phase boundary is indicated by dashed curves in Fig. 2.

The first main result of this work is the experimental observation of the predicted delocalized lobes in the region $|\Delta/J_{\text{eff}}| < 2$. The data clearly exhibit a drive-amplitude-dependent localization-delocalization phase transition, featuring metallic lobes separated by fingers of an insulating phase touching the y axis at the zeroes of the Bessel function $\mathcal{J}_0(K_0)$ where $J_{\text{eff}} = 0$. The analytic $\Delta/|J_{\text{eff}}| = 2$ curves correspond very well to the transition observed both in experimental expansion data (Fig. 2(a) and Fig. 2(b)) and in numerically calculated (IPR) (Fig. 2(c) and Fig. 2(d)). The transition between phases is intrinsically somewhat less sharp when measuring width σ rather than (IPR), because the measured σ scales strongly with the effective hopping time $\hbar/|J_{\text{eff}}|$ even in delocalized regions. The form of the measured high-frequency phase diagram of Fig. 2(a) agrees with both numerical theory (Fig. 2(b)) and analytic approximation, indicating that these data constitute observation of the phase boundaries arising from the interplay between quasi-disorder and driving.

For lower drive frequencies, comparable to the bandwidth, new features appear in both the experimental and numerical phase diagrams which are not captured by the model of Eq. (2). The observation and characterization of these new features constitutes the second main result of this work. These differences are apparent in Figs. 2(b) and 2(d). To visualize the differences, in Fig. 3(a) we show the ratio between the data presented in Fig. 2(b)

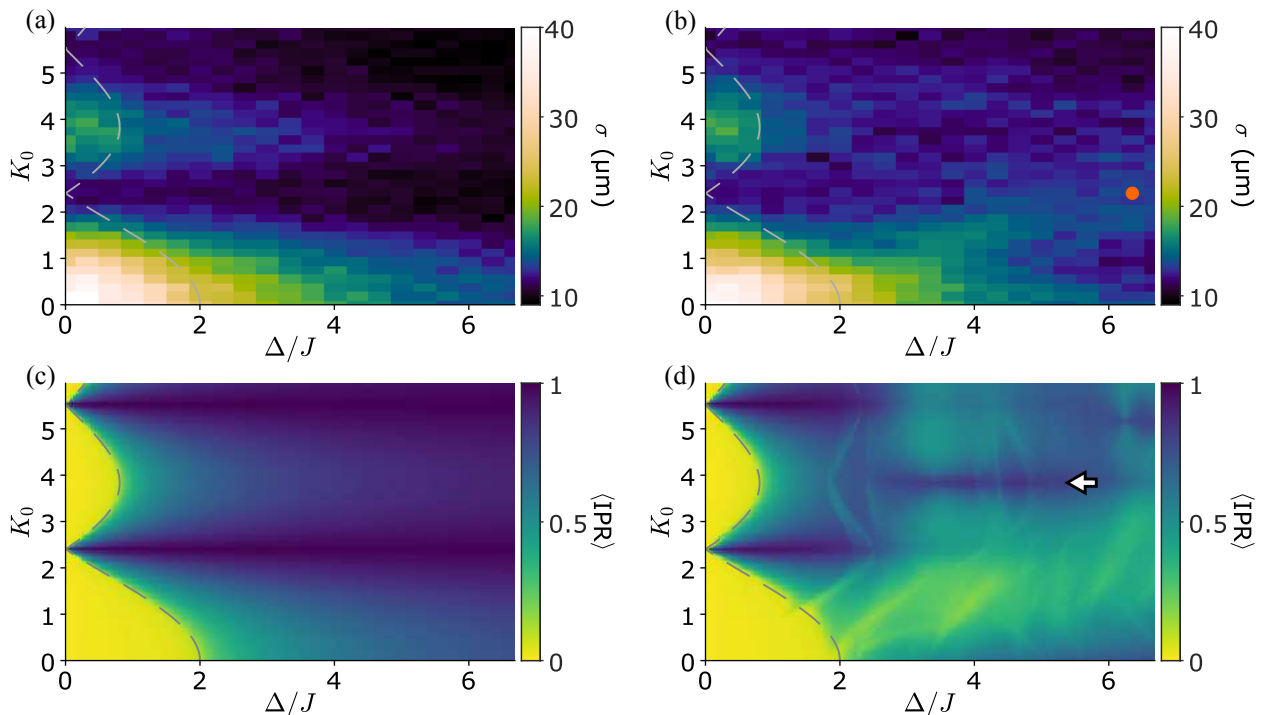


FIG. 2. Interplay of dynamic localization and quasisorder-induced localization in two different drive frequency regimes. **(a)** Measured width σ (standard deviation of a Gaussian fit) of the atomic density distribution after a 500 ms hold, for a high drive frequency $\omega = 2\pi \times (1 \text{ kHz}) = 19.7J/\hbar$. **(b)** Same quantity for a lower drive frequency $\omega = 2\pi \times (200 \text{ Hz}) = 3.93J/\hbar$, near the width of the ground band. The orange dot marks the experimental condition in Fig. 4. **(c)** and **(d)** show numerically calculated average Floquet eigenstate IPR for the 1 kHz drive and the 200 Hz drive respectively. In all panels dashed lines indicate phase boundaries predicted by the approximate model described in the text. In the region $\Delta/J > 2$, we observe clear differences between **(a)** and **(b)** and between **(c)** and **(d)**, indicating differing Floquet eigenstate properties in the two frequency regimes. $V_p = 9E_{R,p}$ for all panels. The white arrow in **(d)** indicates the observed region of enhanced localization, and corresponds to the arrow in Fig. 3(a).

and Fig. 2(a), denoted $\sigma_{200\text{Hz}}/\sigma_{1\text{kHz}}$. We observe the dominant deviation from the high-frequency behavior to occur when $\Delta/J \gtrsim 2$. We note in particular two features, which appear in both the experimental data of Fig. 2(b) and 3(a) and the numerical results of Fig. 2(d): a narrow band of anomalously low expansion near the line $K_0 \approx 3.8$ for larger values of Δ/J , and a broad area of anomalously high expansion in the lower-right of the parameter space. We interpret these features as a signature of nontrivial phenomena not captured by the simple high-frequency approximation.

To further investigate the drive frequency dependence of these features of the phase diagram, we took similar measurements of the expansion with a drive frequency of 300 Hz ($\hbar\omega = 5.90J$), but otherwise identical experimental conditions. The ratio between the measured widths at 300 Hz and the 1 kHz data set, denoted $\sigma_{300\text{Hz}}/\sigma_{1\text{kHz}}$, appears in Fig. 3(b). We observe the same general features at this slightly higher drive frequency, but the extent and magnitude of the deviation is reduced, indicating the approach towards the high-frequency limit.

The first anomalous feature of the low-drive-frequency phase diagram, the observed enhanced localization near

$K_0 \approx 3.8$, corresponds closely to a zero of the *first* Bessel function $\mathcal{J}_1(K_0)$. To better understand this observation, we first note that a gauge transformation takes the oscillating linear force into an oscillating phase in the tunneling strength [18]. The transformed Hamiltonian reads

$$H \rightarrow H' = \sum_l -J (e^{iK_0 \sin \omega t} |l+1\rangle\langle l| + \text{h.c.}) + \Delta \cos(2\pi\beta l - \delta) |l\rangle\langle l|. \quad (3)$$

The effect of the oscillating phase can be captured by the Jacobi-Anger expansion

$$e^{iK_0 \sin \omega t} = \sum_{m=-\infty}^{\infty} \mathcal{J}_m(K_0) e^{im\omega t}.$$

In the high frequency limit, the nonzero-frequency Bessel terms average away over many cycles. However, when $\hbar\omega \approx 4J$, higher-order terms contribute, with the $\mathcal{J}_1(K_0)$ term the most relevant term past leading order. We thus interpret the observed localized stripe near $K_0 \approx 3.8$, indistinguishable within experimental error from the first zero of the \mathcal{J}_1 Bessel function near 3.8317, as the effect

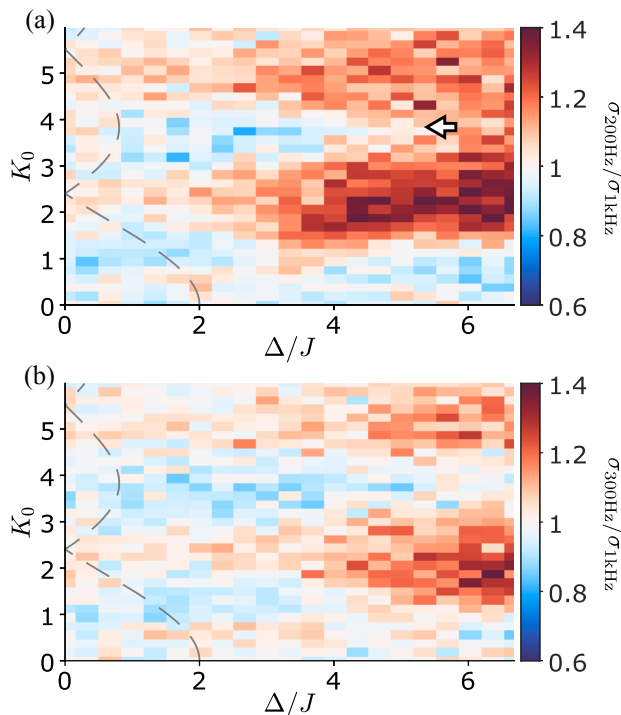


FIG. 3. Measured ratio between high and low frequency phase diagrams. (a) Ratio between the expansion with drive frequency $\omega = 2\pi \times (200 \text{ Hz}) = 3.93J/\hbar$ and $\omega = 2\pi \times (1 \text{ kHz}) = 19.7J/\hbar$. The data used to generate (a) is the same as that presented in Fig. 2. (b) Ratio between data taken at drive frequency $\omega = 2\pi \times (300 \text{ Hz}) = 5.90J/\hbar$ and the same 1 kHz data. The white arrow in (a) is the same as that in Fig. 2(d) and indicates the observed region of enhanced localization.

of a beyond-leading-order localization process not captured in the commonly-used high-frequency approximate description of dynamical localization.

$\omega/2\pi$ (kHz)	0	0.2	0.3	0.4	1
γ	0.24(5)	0.26(5)	0.26(7)	0.12(6)	0.03(21)

TABLE I. Transport exponents γ extracted by fitting the expansion of the condensate in a quasiperiodic lattice under various driving frequencies. Error bars represent 95% confidence interval.

The second anomalous feature, the apparent decrease in localization in the lower-right quadrant of the low-drive-frequency phase diagram, requires a separate explanation. This feature could in principle arise from true delocalization of the Floquet eigenstates or even an extended critical phase. However, as discussed below, additional measurements of transport dynamics and numerical calculations of the IPR of the Floquet eigenstates indicate that this region in fact remains a localized phase in the presence of driving, but with an increased localization length.

To explore the nature of this region of the phase diagram, we experimentally measure the evolution of the

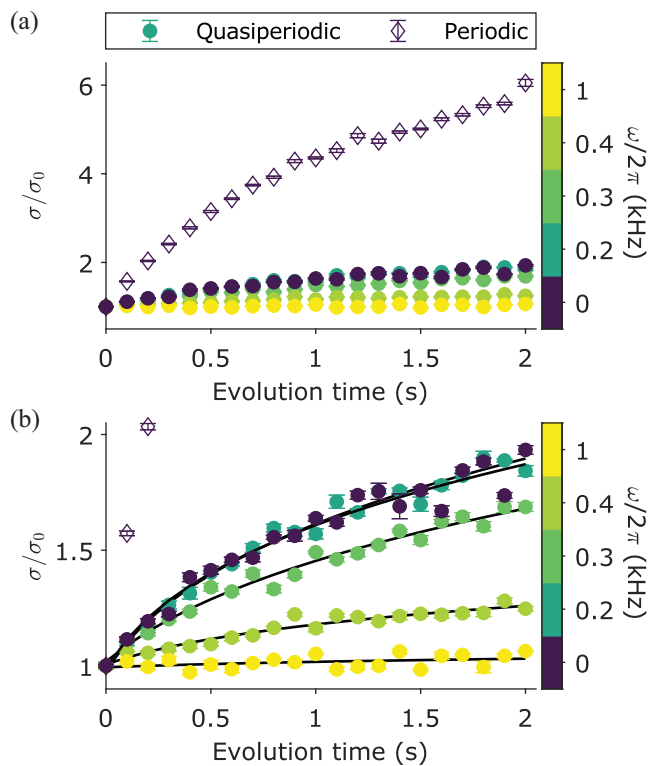


FIG. 4. Measured expansion versus time in various regimes. (a) Expansion in a purely periodic lattice (diamond markers) is much more rapid than that in the quasiperiodic lattice in the localized phase (circular markers). (b) Same data as in (a) with y axis expanded to show variation among the expansions in quasiperiodic potentials. Different driving frequencies are represented by the color of the marker. Each data point is averaged from 5 experimental realizations. Here $\Delta/J = 6.35$ and $K_0 \approx 2.4046$. Error bars show standard error of the mean.

density distribution of the condensate at various driving frequencies, for hold times up to 2 seconds ($\approx 639.4\hbar/J$). In particular, we focus on the case of a strong quasiperiodic potential ($\Delta/J \approx 6.35$) and a driving amplitude of $K_0 \approx 2.4046$. Here, in the absence of periodic driving, the non-interacting system is in the localized phase; without the quasiperiodic potential, the system is near dynamic localization ($\mathcal{J}_0(K_0) = 1.3 \times 10^{-4}$). The results of transport measurements shown in Fig. 4 characterize the interplay between quasisorder-induced and dynamic localization in this regime. We extract the transport exponent γ by fitting the measured evolution to the form $\sigma(t) = \sigma_0(1+t/t_0)^\gamma$ for the quasiperiodic cases [24]. Here σ_0 is the initial width, and t_0 acts as an activation time. Localization, diffusion, and ballistic expansion correspond to $\gamma = 0, 0.5$, and 1 , respectively. We do not fit the periodic case ($\Delta = 0$) to this form, since the residual axial trapping from the lattice beam complicates the dynamics at long evolution time. We benchmark the expansion of the condensate in two cases: a static periodic

lattice and a static quasiperiodic lattice. The evolution in the periodic lattice (diamond markers in Fig. 4(a)) shows the typical fast expansion. In the quasiperiodic, localized case (Fig. 4(b)), the expansion exhibits slow subdiffusion with a transport exponent $\gamma = 0.24(5)$. This sub-diffusion in the localized regime is caused by the finite mean-field interaction inherent to our condensate, as found in previous studies [24, 25].

Fig. 4(b) shows the expansion dynamics in the quasiperiodic lattice with various driving frequencies. When the driving frequency is low, as in the $\omega = 2\pi \times 200$ Hz case, the measured evolution follows that of the static quasiperiodic system. As the driving frequency increases, the width evolution remains subdiffusive and becomes slower. Notably, the expansion is totally arrested within the experimental time in the high-frequency case ($\omega = 2\pi \times 1$ kHz). In all the cases reported, the measured expansion is slower than the undriven quasiperiodic case, which is in the localized phase.

These experimental results imply that the anomalous region in the lower-right of the phase diagram is still a localized phase. We corroborate this with numerical studies of the single-band model (Eq.1). For these numerical studies, we fix $K_0 \approx 2.4046$, the same as the experimental condition in Fig.4, but vary the quasisorder strength Δ . We numerically diagonalize the time-dependent Hamiltonian (Eq.1) via the Floquet formalism, and calculate the IPR of the eigenstates in the central Floquet-Brillouin zone. The scaling of the IPR versus system size distinguishes the phases. Our calculation of the IPR scaling in the Supplementary Information [14] shows only a localized phase without any mobility edges.

What then distinguishes the anomalous region observed in experiment? We argue that this region features localization lengths which are both quantitatively larger and much more quasi-energy dependent than in the high-frequency phase diagram. Numerically calculated values of IPR in the low-frequency case are smaller than those in the high-frequency case (Fig. 5b), meaning that the localization lengths in the low-frequency regime are larger. Past numerical studies showed that localization lengths increase under low-frequency driving for a tight-binding lattice with a truly random disorder [26]. Our calculations thus generalize this result to a quasiperiodic system in the localized phase. The IPR of the low-frequency Floquet eigenstates also varies with quasienergy, as shown in Fig. 5(a) and discussed from a different perspective in [14]. This is in stark contrast to the static AAH model or the high-frequency approximation of the driven case in which the localization length of the eigenstates, and thus their IPR, are independent of the (quasi-)energy [6]. Therefore, although the expansion of the condensate in the low-frequency regime resembles that of the static quasiperiodic lattice, their mechanisms are completely different.

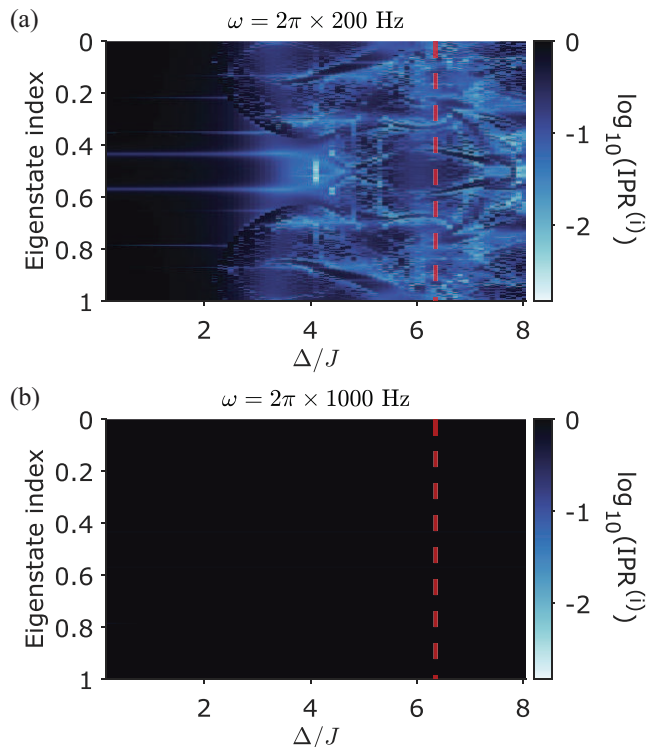


FIG. 5. IPR of Floquet eigenstates in the central Floquet-Brillouin zone in (a) low and (b) high-frequency regimes. Values of IPR of each eigenstate fluctuate heavily for the low-frequency case in (a), but they are independent of each eigenstate in the high-frequency case in (b) up to numerical precision and finite-size effects. The red dashed lines correspond to the quasiperiodic strength Δ/J used in the experiments in Fig. 4.

In summary, we have experimentally and theoretically investigated the interplay of dynamic and quasisorder-induced localization. In the high-frequency regime, the measured phase diagram is consistent with both numerical and time-averaged analytic theory, featuring metallic Bessel lobes separated from insulating regions by a phase boundary which depends on both drive strength and quasisorder strength. For lower frequency driving, comparable to the natural energy scale of the system, we observe localization behavior not captured by the simple time-averaged analytic model, including areas of both enhanced and suppressed transport, and show that it can be understood via extensions to that simple model. This work touches on some of the rich structures that can arise when quantum systems are driven at frequencies near their natural bandwidth, which may prove relevant for future Floquet engineering applications where optimal system parameters deviate from the simple high frequency model. A natural direction for future work is the addition of tunable interactions, enabling experimental probes of the interplay among three distinct fundamental localizing mechanisms of many-body quan-

tum matter: interactions, driving, and disorder [27].

We acknowledge helpful conversations with Martin Holthaus, and research support from the Air Force Office of Scientific Research (FA9550-20-1-0240) and the NSF QLCI program (OMA-2016245). A.R.D. acknowledges support from the UC Santa Barbara NSF Quantum Foundry funded via the Q-AMASE-i program under Grant DMR1906325. The optical lattices used herein were developed in work supported by the U.S. Department of Energy, Office of Science, National Quantum Information Science Research Centers, Quantum Science Center.

* Equal contribution.

† weld@ucsb.edu

- [1] F. Alet and N. Laflorencie, *Comptes Rendus Physique* **19**, 498 (2018).
- [2] R. Moessner and S. L. Sondhi, *Nature Physics* **13**, 424 (2017).
- [3] D. A. Abanin, E. Altman, I. Bloch, and M. Serbyn, *Rev. Mod. Phys.* **91**, 021001 (2019).
- [4] P. Sierant, M. Lewenstein, A. Scardicchio, L. Vidmar, and J. Zakrzewski, Many-body localization in the age of classical computing (2024), arXiv:2403.07111 [cond-mat.dis-nn].
- [5] M. Holthaus, *Phys. Rev. Lett.* **69**, 351 (1992).
- [6] S. Aubry and G. André, *Ann. Israel Phys. Soc.* **3**, 18 (1980).
- [7] G. Roati, C. D’Errico, L. Fallani, M. Fattori, C. Fort, M. Zaccanti, G. Modugno, M. Modugno, and M. Inguscio, *Nature (London)* **453**, 895 (2008).
- [8] Y. Lahini, R. Pugatch, F. Pozzi, M. Sorel, R. Morandotti, N. Davidson, and Y. Silberberg, *Phys. Rev. Lett.* **103**, 013901 (2009).
- [9] M. Holthaus, G. H. Ristow, and D. W. Hone, *Phys. Rev. Lett.* **75**, 3914 (1995).
- [10] M. Holthaus and D. W. Hone, *Philos. Mag. B* **74**, 105 (1996).
- [11] K. Drese and M. Holthaus, *Phys. Rev. Lett.* **78**, 2932 (1997).
- [12] S. Arlinghaus, M. Langemeyer, and M. Holthaus, in *Dynamical Tunneling: Theory and Experiment*, edited by S. Keshavamurthy and P. Schlagheck (CRC Press, 2011) 1st ed., Chap. 12.
- [13] D. Guzman-Silva, M. Heinrich, T. Biesenthal, Y. V. Kartashov, and A. Szameit, *Opt. Lett.* **45**, 415 (2020).
- [14] See Supplementary Material for experimental and theoretical details, which includes Ref. [27–30].
- [15] X. Li, X. Li, and S. Das Sarma, *Phys. Rev. B* **96**, 085119 (2017).
- [16] M. Modugno, *New Journal of Physics* **11**, 033023 (2009).
- [17] S. Y. Jitomirskaya, *Annals of Mathematics* **150**, 1159 (1999).
- [18] A. Eckardt, C. Weiss, and M. Holthaus, *Phys. Rev. Lett.* **95**, 260404 (2005).
- [19] R. Graham, M. Schlautmann, and P. Zoller, *Phys. Rev. A* **45**, R19 (1992).
- [20] K. W. Madison, M. C. Fischer, R. B. Diener, Q. Niu, and M. G. Raizen, *Phys. Rev. Lett.* **81**, 5093 (1998).
- [21] H. Lignier, C. Sias, D. Ciampini, Y. Singh, A. Zenesini, O. Morsch, and E. Arimondo, *Phys. Rev. Lett.* **99**, 220403 (2007).
- [22] M. Holthaus, *J. Phys. B* **49**, 013001 (2016).
- [23] C. M. Le, R. Akashi, and S. Tsuneyuki, *Phys. Rev. A* **105**, 052213 (2022).
- [24] E. Lucioni, B. Deissler, L. Tanzi, G. Roati, M. Zaccanti, M. Modugno, M. Larcher, F. Dalfovo, M. Inguscio, and G. Modugno, *Phys. Rev. Lett.* **106**, 230403 (2011).
- [25] T. Shimasaki, M. Prichard, H. E. Kondakci, J. E. Pagett, Y. Bai, P. Dotti, A. Cao, A. R. Dardia, T.-C. Lu, T. Grover, and D. M. Weld, *Nature Physics* 10.1038/s41567-023-02329-4 (2024).
- [26] D. F. Martinez and R. A. Molina, *Phys. Rev. B* **73**, 073104 (2006).
- [27] E. Bairey, G. Refael, and N. H. Lindner, *Phys. Rev. B* **96**, 020201 (2017).
- [28] R. Walters, G. Cotugno, T. H. Johnson, S. R. Clark, and D. Jaksch, *Phys. Rev. A* **87**, 043613 (2013).
- [29] D. J. Thouless, *Journal of Physics C: Solid State Physics* **5**, 77 (1972).
- [30] B. Kramer and A. MacKinnon, *Reports on Progress in Physics* **56**, 1469 (1993).

Supplementary Material: Localization phase diagram controlled by the interplay of disorder and driving

Peter Dotti, Yifei Bai, Toshihiko Shimasaki, Anna R. Dardia, and David Weld
Department of Physics, University of California, Santa Barbara, California 93106, USA
(Dated: June 4, 2024)

EXPERIMENTAL DETAILS AND TIGHT-BINDING MODEL PARAMETERS

The experiments described in the main text begin by loading a Bose-Einstein condensate of ^{84}Sr atoms, numbering 8×10^4 atoms, into a pair of superimposed coaxial 1D optical lattices with different spatial periods, aligned along an axis perpendicular to gravity. The deeper of these two lattices is referred to as the primary lattice. It is generated by counterpropagating laser beams with wavelength $\lambda_p = 1064$ nm. The two primary lattice beams are derived from the same fiber amplifier, but their frequency and amplitude can be tuned independently using acousto-optic modulators (AOMs). One of the primary lattice beams has a much higher intensity than any of the other beams (approximately 2 W) in order to support the atoms against gravity. The depth of the primary lattice V_p can be controlled by adjusting the intensity and polarization of the weaker beam. V_p is maintained to be constant with feedback to power monitoring photodiodes for each of the beams. These conditions of relatively weak transverse confinement result in sufficiently low atom cloud densities such that interactions can be neglected in our experimental models.

All experiments in this work were conducted with $V_p = 9E_{R,p}$, where $E_{R,p} = \hbar^2 k_p^2 / 2m$ and $k_p = 2\pi / \lambda_p$. The depth of the primary lattice was calibrated to be accurate within 5% of the nominal value of $9E_{R,p}$ by checking the resonant transition frequency between the ground state of the lowest band and the highest energy state of the first excited band for atoms loaded into the lattice using a sinusoidal translation of the lattice at several frequencies near resonance and observing reduction in atom density that occurs when the atoms are resonantly excited. The translation amplitude corresponded to an amplitude in frequency difference of 40 Hz ($\Delta\nu_{\text{max},p} = 40$ Hz) between the two primary lattice beams. The secondary lattice depth was calibrated to an accuracy of 5% using Kapitza-Dirac diffraction of the atom cloud initially held in the strong beam of the primary lattice. We estimated the radial and axial trapping frequencies are $\omega_r = 2\pi \times 100.1$ Hz and $\omega_z = 2\pi \times 0.3067$ Hz, respectively.

The two laser beams that form the secondary lattice have wavelength $\lambda_s = 874.6$ nm and are derived from a continuous wave titanium sapphire laser stabilized against drift with a wavemeter. The secondary lattice beams are of roughly equal intensity, are stabilized with monitoring photodiodes, and are adjusted together to control the depth of the secondary lattice V_s . These beams have independently AOM-tunable frequencies as with the primary lattice. Values of the secondary lattice depth used in the presented experiments range from $0E_{R,p}$ to $0.592E_{R,p}$.

This setup provides fast tunability of the potential depths and translation of the optical lattice potentials along the lattice direction, which enables the simultaneous experimental realization of dynamic and quasidisorder-induced localization. The system model is depicted schematically in Fig. 1(a) of the main text and described by the one-dimensional Hamiltonian

$$H_{\text{Exp}} = -\frac{\hbar^2}{2m} \frac{d^2}{dx^2} + V_p \sin^2(k_p(x - \delta_p)) + V_s \sin^2(k_s(x - \delta_s)), \quad (1)$$

where V_p and V_s are the depths of the primary and secondary lattice, respectively. $k_{p(s)} = 2\pi / \lambda_{p(s)}$ and $\delta_{p(s)}$ denotes the possibly time-dependent spatial offset of the of the primary (secondary) lattice, which is determined by the phase difference $\Delta\varphi_{p(s)}$ between the counterpropagating laser beams according to the formula

$$\delta_{p(s)} = \frac{\Delta\varphi_{p(s)}}{2k_{p(s)}}. \quad (2)$$

The velocity of each lattice is thus

$$v_{p(s)} = \frac{d}{dt} \delta_{p(s)} = \frac{\lambda_{p(s)}}{2} \Delta\nu_{p(s)}, \quad (3)$$

where $\Delta\nu_{p(s)}$ is the frequency difference between the two laser beams forming the primary (secondary) lattice. We directly control $\Delta\nu_{p(s)}$ by adjusting the phase of the radio frequency (RF) drive to the AOM. All RF waveform

generators share a clock signal so that the relative position of the two lattices is well controlled up to unavoidable thermal drift of optical path lengths due to opto-mechanical element drift and index of refraction changes that are unimportant on the time scale of the collection of individual data points, but can change the relative positions of the lattices between runs. This effectively results in averaging over system realizations with different initial positions (δ_p and δ_s at the initial time) of the lattice in the experimental data. The time evolution behavior is expected generically to be insensitive to this relative lattice position change, and the data does not measurably change as a result of this drift.

We specialize this paper to synchronized sinusoidal driving of the primary and secondary lattices, so that

$$\delta_p = \delta_s + \delta_0 = -A \cos(\omega t) \quad (4)$$

where δ_0 is constant over the time scale of each experimental run. As stated in the text, we use as our model Hamiltonian the tight-binding model approximation corresponding to Hamiltonian (1), given as [1]

$$H = \sum_l -J \left[|l+1\rangle\langle l| + |l\rangle\langle l+1| \right] + \Delta \sum_l \cos(2\pi\beta l - \delta) |l\rangle\langle l| + \hbar\omega K_0 \cos(\omega t) \sum_l l |l\rangle\langle l|, \quad (5)$$

where J is the tunneling energy, Δ is the quasidisorder strength, K_0 is the dimensionless drive strength, $\beta = \lambda_p/\lambda_s = 1064/874.61$ and $\delta = 2\delta_0/\lambda_p$. This Hamiltonian describes the system in the reference frame that is co-moving with the primary lattice, i.e. the primary lattice is stationary in this frame. The Hamiltonian in the comoving frame is related to the lab frame by a unitary transformation, consideration of which produces the following relations between K_0 and drive amplitude.

$$K_0 \frac{\hbar\omega}{(\lambda_p/2)} = mA\omega^2 = \frac{m\lambda_p\omega}{2} \Delta\nu_{\max,p}. \quad (6)$$

Here, $\Delta\nu_{\max,p}$ is the experimentally relevant amplitude in frequency difference between the the laser beams forming the primary lattice, i.e. $\Delta\nu_p = \Delta\nu_{\max,p} \sin(\omega t)$. Each ground band Wannier state $|l\rangle$ corresponds to the state localized at the position $x_l = l\pi k_p + \delta_p$. Wannier states are computed numerically to determine J and Δ [2]. For $V_p = 9E_{R,p}$, we have $J = 0.0242E_{R,p}$, and for the range of V_s values, Δ ranges from $0E_{R,p}$ to $0.162E_{R,p}$.

Localization properties are observed experimentally via measured width, using the standard deviation σ of a best-fit Gaussian to the 1D transversely-integrated density distribution along the lattice axis. In the measured phase diagrams in the main text, the average fitted σ of three repeats is shown for each pair of K and Δ/J values, except in rare (0.1%) outlier cases in which atom loss resulted in a poor fit, in which cases the remaining two repeats were averaged.

CALCULATION AND SCALING OF THE INVERSE PARTICIPATION RATIO

Here we discuss the calculation of the Floquet eigenstates and their inverse participation ratio.

For a time-periodic Hamiltonian $H(t) = H(t+T)$ where T is the period, there exists a complete and orthonormal basis $\{|\psi_n(t)\rangle\}$. We refer to the elements of this basis set $|\psi_n(t)\rangle$ as Floquet eigenstates. In analogy to the Bloch state in a spatially periodic system, the Floquet eigenstate can be decomposed into a product of a plane wave $e^{-i\varepsilon_n t}$ and a time-periodic ‘‘Floquet function’’ $|\Phi_n(t)\rangle$ as $|\psi_n(t)\rangle = e^{-i\varepsilon_n t} |\Phi_n(t)\rangle$, where ε_n is the quasienergy of the Floquet eigenstate.

The Floquet function has the same time-periodicity of the Hamiltonian: $|\Phi_n(t)\rangle = |\Phi_n(t+T)\rangle$. We can thus apply the discrete Fourier transform to $|\Phi_n(t)\rangle$ and $H(t)$ as

$$H(t) = \sum_{m=-\infty}^{\infty} e^{-im\omega t} H_m, \quad |\Phi_n(t)\rangle = \sum_{m=-\infty}^{\infty} e^{-im\omega t} |\phi_{m,n}\rangle.$$

where $\omega = 2\pi/T$. Once we substitute the discrete Fourier transform into the time-dependent Schrödinger equation, we arrive at a time-independent equation for each Fourier component as

$$(\varepsilon_n + m\hbar\omega) |\phi_{m,n}\rangle = \sum_{m'=-\infty}^{\infty} H_{m-m'} |\phi_{m',n}\rangle. \quad (7)$$

We can then obtain quasienergies and Floquet eigenstates by numerically diagonalizing Eq. (7) followed by the inverse discrete Fourier transform at time t . In this work we take $t = 0$. In analogy to the Brillouin zone in the extended

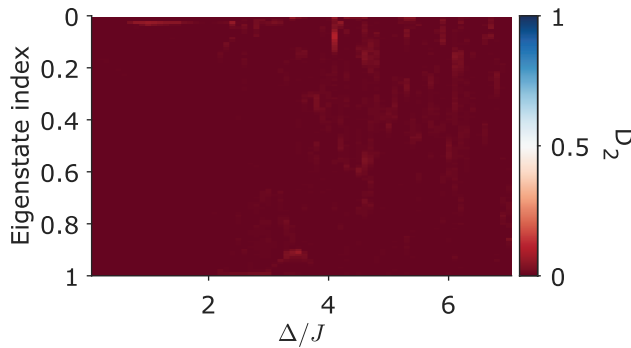


FIG. 1. Fractal dimensions of Floquet eigenstates at $K_0 = 2.4046$.

scheme, the solution of Eq. (7) has infinitely-many identical copies of the same Floquet eigenstates, leading to the concept of Floquet-Brillouin zones. We consider the Floquet eigenstates and quasienergy in the central Floquet-Brillouin zone ($m = 0$) for the main text and remainder of the discussion. Finally, for a realistic numerical study, we can only include finitely many Floquet-Brillouin zones. The summation in Eq. (7) includes terms up to some cutoff m_{cutoff} .

We will now discuss our specific Hamiltonian of interest (Eq. (1) in the main text). We first apply a unitary gauge transformation to the driven AAH Hamiltonian as:

$$H \rightarrow H' = -J \sum_l \left[e^{iK_0 \sin(\omega t)} |l+1\rangle\langle l| + e^{-iK_0 \sin(\omega t)} |l\rangle\langle l+1| \right] + \Delta \sum_l \cos(2\pi\beta l - \delta) |l\rangle\langle l|.$$

The Fourier components of the transformed Hamiltonian $H' = \sum_m e^{-im\omega t} H_m$ is given by the Jacobi-Anger expansion

$$H_m = -J \sum_l \left[\mathcal{J}_m(K_0) |l+1\rangle\langle l| + \mathcal{J}_{-m}(K_0) |l\rangle\langle l+1| \right] + \begin{cases} \Delta \sum_l \cos(2\pi\beta l - \delta) |l\rangle\langle l|, & m = 0, \\ 0, & m \neq 0. \end{cases}$$

The $m = 0$ term corresponds to the time-averaged Hamiltonian. We can then substitute H_m to Eq. (7) and obtain the quasienergies and Floquet eigenstates.

We use the inverse participation ratio (IPR) in the position basis to probe the localization property of the Floquet eigenstates. After projecting the Floquet eigenstate $|\psi_i\rangle$ to the position basis as $|\psi_i\rangle = \sum_l \psi_l^{(i)} |l\rangle$, its IPR for the i^{th} eigenstate is then defined as

$$\text{IPR}^{(i)} = \frac{\sum_{l=1}^L |\psi_l^{(i)}|^4}{\left(\sum_{l=1}^L |\psi_l^{(i)}|^2\right)^2}. \quad (8)$$

Here L is the system size. A localized (delocalized) wavefunction has a non-vanishing (vanishing) value of IPR.

Furthermore, scaling the IPR with respect to the system size L allows us to distinguish the phases without relying on the numerical values of IPR. The IPR scales as

$$\text{IPR}^{(i)} \sim L^{-D_2}.$$

D_2 is called the fractal dimension. When $D_2 = 0(1)$, the state is localized (delocalized). When $0 < D_2 < 1$, the state is critical with multifractal characteristics.

We computed D_2 at $K_0 = 2.4046$ and $\omega = 2\pi \times 200$ Hz. The result in Fig. 1 shows that all the Floquet eigenstates are localized without any mobility edges or critical states. Thus we cannot explain the observed low-frequency deviation with anomalous localization observed in [3].

ENERGY-DEPENDENT LOCALIZATION LENGTH WITH THE FLOQUET-GREEN FORMALISM

Here we include numerical calculation of the localization length of the driven AAH model. We vary the quasiperiodic strength Δ/J and fix $K_0 \approx 2.4046$, the same as the experimental condition for Fig. 4 in the main text.

The localization length is computed via the Floquet-Green formalism [4]. We first recall some basic definitions and background before discussing the actual calculation. We start with a 1D, time-independent lattice system of length L and a particle with energy E . The system can be captured by its Green's function $G(E)$. The localization length of the system $\xi(E)$ can then be defined as [5]

$$\frac{1}{\xi(E)} = - \lim_{L \rightarrow \infty} \frac{1}{L} \langle \ln |G_{1,L}(E)| \rangle,$$

where $G_{1,L}(E)$ is the matrix element of the Green's function at $(1, L)$. Here $\langle \cdot \rangle$ represents averaging over different potential realizations. One can relate this quantity to the transmission from the beginning of the lattice at site 1 to the end at the site L . From this interpretation, E need not be the eigenenergy of the system. From this definition, it is then straightforward to show that the localization length of the static AAH model is $\xi^{-1} = \ln(\Delta/(2J))$ [6, 7].

The generalization of the Green's function to a time-periodic system was discussed in [4]. We consider the Hamiltonian

$$\hat{H}(t) = \hat{H}_{\text{static}} + 2\hat{V} \cos \omega t.$$

The factor of 2 is for convenience only. For our model under study, \hat{H}_{static} is the static AAH model, and $\hat{V} := \hbar\omega K_0/2 \sum_l |l\rangle\langle l|$ represents the oscillating dipolar force.

The Floquet-Green's function can then be defined with the Fourier components of the Floquet eigenstates

$$G^{(k)}(E) = \sum_{n,m} \frac{|\phi_{m+k,n}\rangle \langle \phi_{m,n}|}{E - \epsilon_n - m\hbar\omega}$$

Similarly to the undriven case, the matrix element $G_{1,L}^{(k)}(E)$ of the Floquet-Green's function relates to the transmission of a particle with energy E through the driven lattice system: the particle enters the lattice with energy E and leaves with energy $E + m\hbar\omega$. The integer k thus labels such a transmission channel.

Thus, we can extend the definition of the localization length as

$$\frac{1}{\xi^{(k)}(E)} = - \lim_{L \rightarrow \infty} \frac{1}{L} \langle \ln |G_{1,L}^{(k)}(E)| \rangle. \quad (9)$$

It can be shown that $\xi^{(k)}(E)$ are all equal for different integer k . Furthermore, in the limit of vanishing driving $\hat{V} \rightarrow 0$, $G^{(k=0)}(E) \rightarrow G(E)$ and $G^{(k \neq 0)}(E) \rightarrow 0$. Therefore, we can restrict the calculation to $G^{(0)}(E)$ and consider $\xi^{(0)}$ only.

The Floquet-Green function $G^{(0)}(E)$ satisfies [4]

$$G^{(0)}(E) = \frac{1}{E\hat{I} - \hat{H}_{\text{static}} - \hat{V}_{\text{eff}}(E)}, \quad \hat{V}_{\text{eff}}(E) = \hat{V}_{\text{eff}}^+(E) + \hat{V}_{\text{eff}}^-(E), \quad (10)$$

where the dynamical effective potential can be evaluated by a matrix continued fraction

$$\hat{V}_{\text{eff}}^{\pm}(E) = \hat{V} \frac{1}{(E \pm 1\hbar\omega)\hat{I} - \hat{H}_{\text{static}} - \hat{V} \frac{1}{(E \pm 2\hbar\omega)\hat{I} - \hat{H}_{\text{static}} - \hat{V}^{\pm} \hat{V}} \hat{V}} \hat{V}. \quad (11)$$

$$\vdots$$

In practice, we choose $L = 100$ and iterate the continued fraction 200 times to ensure convergence. We choose $\delta = 0$ in our calculations.

We present the result for $\omega = 2\pi \times 200$ Hz in Fig. 2. At $K_0 \approx 2.4046$, we expect the localization length to essentially vanish within the high-frequency approximation. This is because the effective quasiperiodic strength $\Delta/(J\mathcal{J}_0(K_0))$ diverges as K_0 approaches to the zeroes of $\mathcal{J}_0(K_0)$. We observe that the localization lengths are energy dependent at $\omega = 2\pi \times 200$ Hz and are larger than the high-frequency prediction. This corroborates the same results but drawn from the IPR calculation.

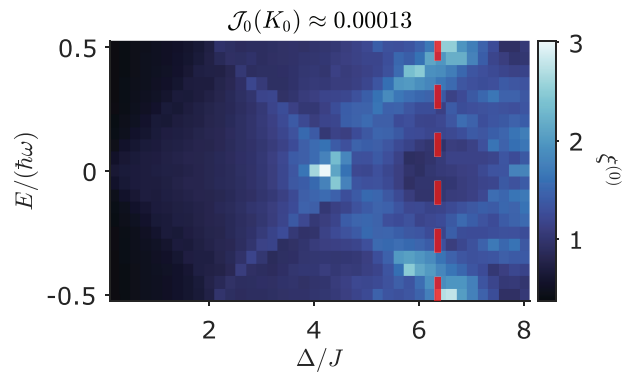


FIG. 2. Localization length at $\omega = 2\pi \times 200$ Hz and $K_0 = 2.4046$ in units of the lattice spacing. The dashed red line shows the quasiperiodic strength at which the experiments shown in Fig. 4 in the main text were conducted.

-
- [1] K. Drese and M. Holthaus, Phys. Rev. Lett. **78**, 2932 (1997).
 - [2] R. Walters, G. Cotugno, T. H. Johnson, S. R. Clark, and D. Jaksch, Phys. Rev. A **87**, 043613 (2013).
 - [3] T. Shimasaki, M. Prichard, H. E. Kondakci, J. E. Pagett, Y. Bai, P. Dotti, A. Cao, A. R. Dardia, T.-C. Lu, T. Grover, and D. M. Weld, Nature Physics 10.1038/s41567-023-02329-4 (2024).
 - [4] D. F. Martinez and R. A. Molina, Phys. Rev. B **73**, 073104 (2006).
 - [5] B. Kramer and A. MacKinnon, Reports on Progress in Physics **56**, 1469 (1993).
 - [6] D. J. Thouless, Journal of Physics C: Solid State Physics **5**, 77 (1972).
 - [7] S. Aubry and G. André, Ann. Israel Phys. Soc. **3**, 18 (1980).